

FEATURE ARTICLE

Nonlinear Chemical Imaging Nanomicroscopy: From Second and Third Harmonic Generation to Multiplex (Broad-Bandwidth) Sum Frequency Generation Near-Field Scanning Optical Microscopy**Richard D. Schaller, Justin C. Johnson, Kevin R. Wilson, Lynn F. Lee, Louis H. Haber, and Richard J. Saykally****Department of Chemistry, University of California, Berkeley, California 94720-1460**Received: December 10, 2001; In Final Form: February 13, 2002*

The emerging field of coherent nonlinear near-field scanning optical microscopy (NSOM) is reviewed. Second harmonic, third harmonic, and sum frequency generation (SHG, THG, and SFG) are explored as means of providing chemically and environmentally selective probes with nanometer spatial resolution provided by scanning probe microscopy. Chemical selectivity is generated via resonant enhancement of the nonlinear signals, whereas interface vs bulk contrast is achieved by the order (even vs odd) of the optical process. A method of producing higher spectral resolution, and thus increased chemical selectivity, is also demonstrated in the form of near-field detected multiplex (or “broad-bandwidth”) SFG (MSFG). Applications to biological and material samples are described.

I. Introduction

Few technological advances have the broad and dramatic impact on science as do those in microscopy. The advent of STM and AFM constitute two poignant examples. In the area of far-field optical microscopy, two-photon fluorescence imaging stands as one of the most important modern advances. The dependence of two-photon fluorescence on the square of the incident laser intensity engenders higher spatial localization of fluorescence intensity than does the linear counterpart, and the use of near-IR excitation lasers minimizes both optical damage and scattering background in the sample.¹ These advantages have proven to be very important for imaging fragile cellular materials and processes.^{2–4}

Over the last two decades, a host of other far-field nonlinear laser spectroscopy technologies have been developed and applied to chemical analysis. These include SHG and SFG (SHG is simply SFG with two degenerate photons), THG, coherent anti-Stokes Raman spectroscopy (CARS), and a variety of related mixing techniques.^{5–7} However, the general exploitation of these powerful methods for sample imaging is only now appearing due to their technical complexity. To date, far-field imaging of both biological and material samples using SHG,^{8–13} SFG,¹⁴ and THG^{13,15–20} has been demonstrated. Recent publications have also reported the development of far-field CARS imaging.^{21–26}

During the past few years we have explored combining NSOM with various nonlinear optical techniques as a means to achieve both chemical specificity and environmental (isotropic or anisotropic) selectivity in subdiffraction spatial resolution imaging. Many of the characteristics of NSOM have now been

explored extensively, as over five hundred publications have appeared to date^{27–29} that utilize NSOM to transcend the far-field diffraction limit on spatial resolution ($\sim \lambda/2$) by probing a sample in the electromagnetic near-zone.³⁰ However, nearly all of these works exploit the linear optical sample response (absorption, reflection/transmission, fluorescence, etc.) in order to extract spatially resolved information from a sample.

Nonlinear optical sample responses have the potential to be a powerful tool in imaging for several reasons. The first is that the magnitude of the nonlinear response of a sample can typically vary by orders of magnitude more than the linear response.^{31–33} This is most clearly demonstrated in the case of linear absorption vs nonlinear harmonic generation, wherein linear absorptions typically vary by ca. 10% in a sample whereas harmonic generation can increase in efficiency by 10^4 with resonant enhancements.³¹ Nonlinear optical experiments can, in many instances, also constitute low background measurements in the same manner as fluorescence because the photons incident on the sample are not at the same frequency as those that are detected. Also, depending on the translational and molecular symmetry of a sample as well as the order of the nonlinear optical process, interfacial (anisotropic) or bulk (isotropic) sensitivity can be obtained within the dipole approximation.³¹

In this work, we explore a variety of coherent nonlinear optical processes and demonstrate that combining resonantly enhanced nonlinear optical processes with NSOM can serve as new chemically selective contrast mechanisms for high spatial resolution imaging. In the long term, we seek to reduce the dependence, especially in biology, on synthetic fluorescent chromophores for sample imaging. Resonantly enhanced nonlinear processes can produce optical contrast in imaging independent of the properties of the final excited state of a molecule (viz., photoemissive or nonphotoemissive), and thereby

* To whom correspondence should be addressed. E-mail: saykally@uclink4.berkeley.edu.

enable the use of nonphotoemissive chromophores for dye-labeled imaging as well as increase the prospects for imaging via intrinsic chromophores. To date, we have reported applications of SHG,³⁴ infrared+visible SFG,³⁵ and THG³⁶ NSOM for imaging both biological and semiconductor material samples. Other groups have also recently published materials studies employing SHG^{37–55} as well as near-infrared+visible SFG⁵⁶ NSOM. Here we review these developments as well as demonstrate some novel techniques, referring to the whole of this rapidly developing field as nonlinear chemical imaging nanomicroscopy (NCIN), since the spatial resolution currently achieved is routinely ~ 100 nm.

The linear induced polarization (P) of a sample is proportional to the incident oscillating electric field (E) via a matrix of proportionality constants (χ), which constitutes the characteristic linear susceptibility of the sample. This approximation

$$P = \epsilon_0 \chi E \quad (1)$$

(ϵ_0 is vacuum permittivity) becomes insufficient to describe the total induced polarization in the sample at very high electromagnetic field intensities (~ 1 MW/cm²), such as achieved routinely with modern pulsed laser systems. Therefore, this expression must be treated more rigorously as a power series expansion.³¹

$$P^{(1)} + P^{(2)} + P^{(3)} + \dots \approx \chi^{(1)}E + \frac{1}{2}\chi^{(2)}EE + \frac{1}{6}\chi^{(3)}EEE + \dots \quad (2)$$

This expansion contains terms that describe the n th-order induced polarization ($P^{(n)}$) which is proportional to the product of an n th-order susceptibility tensor ($\chi^{(n)}$) of rank $n + 1$, and n powers of the incident electric field. The n th-order susceptibility tensors are, again, intrinsic properties of the sample. Substitution of the electric field terms with a monochromatic incident light field, $A \sin \omega t$, results in the expression

$$P_{\text{TOTAL}} \approx \chi^{(1)}A \sin \omega t + \frac{1}{2}\chi^{(2)}A^2 - \frac{1}{2}\chi^{(2)}A^2 \cos 2\omega t - \frac{1}{6}\chi^{(3)}A^3 \sin 3\omega t + \dots \quad (3)$$

where 2ω and 3ω are SHG and THG signals, respectively. Sum ($\omega_1 + \omega_2$) and difference ($\omega_1 - \omega_2$) frequency generation (DFG) signals can also be observed when multiple frequencies of light are coincident upon the sample. CARS ($2\omega_1 - \omega_2$) and other higher order mixing processes can be viewed as combinations of sum and difference frequency mixings.

Environmental selectivity (for isotropic or anisotropic environments) can also be obtained in nonlinear imaging due to different selection rules for even- vs odd-order optical processes.³¹ Within the dipole approximation, even-order processes can only produce a nonzero second-order polarization when molecular and translational inversion symmetries do not exist in the sample. Such even-order processes can thus be selective for anisotropic environments, i.e., interfaces, whereas odd-order processes, which do not have this requirement, are generally sensitive to both isotropic and anisotropic environments.

Chemically selective contrast is produced in NCIN imaging via the resonant component of the n th order susceptibility,

$$\chi_{\text{TOTAL}}^{(n)} = \chi_{\text{R}}^{(n)} + \chi_{\text{NR}}^{(n)} \quad (4)$$

where χ_{NR} , the nonresonant part of the total susceptibility, is essentially wavelength independent and χ_{R} can be described, here for the example of SFG, as³¹

$$\chi_{\text{R}}^{(2)} \approx \sum_{n,n' \neq g} \frac{\langle g|i|n \rangle}{(\omega_{\text{SF}} - \omega_{ng} + i\Gamma_{ng})} \times \left(\frac{\langle n|j|n' \rangle \langle n'|k|g \rangle}{(\omega_1 - \omega_{n'g} + i\Gamma_{n'g})} + \frac{\langle n|k|n' \rangle \langle n'|j|g \rangle}{(\omega_2 - \omega_{n'g} + i\Gamma_{n'g})} \right) \quad (5)$$

Here, when an allowed transition between states (ground, g , and intermediate states, n) occurring at ω_{ng} frequency becomes degenerate with the frequency of an input (ω_1, ω_2) or output ($\omega_{\text{SF}} = \omega_1 + \omega_2$) photon, the denominator of a term approaches zero leaving only the imaginary lifetime of the transition (Γ^{-1}), resulting in a large increase (10^4) in efficiency of the nonlinear process being probed. Such resonant enhancement can effect high contrast, chemically specific imaging due to the chemical character of the transition frequencies involved in the nonlinear optical process (e.g., vibrational or electronic).

NSOM surpasses the far-field diffraction limit of $\sim \lambda/2$ by sampling the near-zone of the electromagnetic fields produced by the sample with a nanoscopically sharpened (typically ~ 50 – 100 nm) fiber optic probe, commonly fabricated by adiabatic pulling,⁵⁷ chemical etching,⁵⁸ and focused ion beam^{59,60} methods. The essential concept of NSOM is to launch light to (illumination mode) or collect light from (collection mode) a sample with an aperture of radius much smaller than the wavelength ($r \ll \lambda$) and positioned at a distance from the sample much less than half the detected wavelength ($d \ll \lambda/2$). Under these conditions, the optical spatial resolution is primarily determined by the aperture diameter.^{27,29,61}

The near-field detected nonlinear signal intensity (I), which is proportional to the square of the generated nonlinear induced polarization, for coherent nonlinear optical processes conducted in oblique collection mode can be expressed as the far-field signal intensity^{31,62,63} attenuated by near-field microscopy terms.²⁹ In the case of SFG the expression is

$$I(\omega_{\text{SF}}) = \frac{8\pi^3(\omega_{\text{SF}})^2}{c^3[\epsilon(\omega_{\text{SF}})\epsilon(\omega_1)\epsilon(\omega_2)]^{(1/2)}} |e_{\text{SF}} \tilde{\chi}^{(2)} : e_{\omega_1} e_{\omega_2}|^2 I(\omega_1) I(\omega_2) \left(\frac{r}{\lambda}\right)^6 \left[\int_0^l e^{-(T+S)/k\lambda} dS\right]^2 \quad (6)$$

and for the case of THG is

$$I(3\omega) = \frac{576\pi^4\omega^2}{c^4\epsilon(\omega)\epsilon(3\omega)} |e_{3\omega} \tilde{\chi}^{(3)} : e_{\omega} e_{\omega} e_{\omega}|^2 I^3(\omega) \left(\frac{r}{\lambda}\right)^6 \left[\int_0^l e^{-(T+S)/k\lambda} dS\right]^2 \quad (7)$$

where $\epsilon(\omega)$ is the material dielectric constant, $e_{\Omega} = L_{\Omega} \hat{e}_{\Omega}$ where \hat{e}_{Ω} indicates the unit polarization vector of the field at frequency Ω and L_{Ω} is the Fresnel factor for the field, $I(\omega)$ is the laser intensity, r is the radius of the probe tip, k is a material-specific barrier to photon tunneling, and λ is the wavelength of the detected photons. The optical transmission efficiency of a subwavelength aperture varies as $(r/\lambda)^6$ and signifies a sacrifice of optical signal for high spatial resolution.^{27,29} The exponential attenuation term models the optical transmission mechanism as a photon tunneling event from the position of the nonlinear field creation event at a distance S from the near-field probe tip to a region within the probe that is of wavelength dimensions at a

distance T from the probe tip.^{29,61,64} It should be noted that the source distance (S) in the exponential term will attenuate signals produced within the detection volume, which is typically approximated as a cylinder of radius r beneath the tip,⁶⁵ as distance from the tip is increased, resulting in the observed depth of field a distance l into the sample. Not explicitly accounted for in Equations 6 and 7 is the effect of phase matching relaxation that should increase observed signal levels by collecting the nonlinear evanescent electric field prior to cancellation by interference in non-phase matched directions in the far-field.^{66,67} Additionally, the Fresnel factors for the exiting of the nonlinear signal ($e_{2\omega}$ and $e_{3\omega}$), have not yet been systematically studied as to their actual behavior in the near-field.⁶⁸

The fiber optic tip is mounted in a scanning, non-contact AFM-like system for precise collection of optical signals as a function of position. Maintenance of near-field feedback conditions simultaneously images the physical topography of the sample.

II. Experimental Considerations and Setup

Although nearly all linear NSOM work has been performed in illumination mode, wherein excitation light is delivered to the sample via the fiber optic and signals produced by the sample are detected in far-field reflection or transmission directions or back through the near-field probe itself (illumination/collection), this method does not lend itself very well to nonlinear optical measurements. While SHG measurements using illumination mode have been demonstrated with some success,^{39,41,42} problems relating to high background levels, rapidly divergent signals, limited incident laser powers,³⁷ and lack of access to surface normal modes of a sample⁸ are presented. High second- and third-order background signals (including self-phase modulation) are created primarily due to the long path length (~ 1 m) and multiple interfacial interactions between the high intensity excitation laser pulse and the fiber optic that eventually forms the nanoscopic tip. Further, the high attenuation (ca. 10^4 – 10^6) that is experienced when the excitation pulse propagates into the subwavelength aperture indicates that vastly higher intensities must be launched into the fiber than will reach the sample, further amplifying the background relative to signal. Moreover, because the excitation pulse rapidly diverges from the probe tip as it develops far-field characteristics,^{27,61} the generated signal photons, which will conserve momentum, will be rapidly divergent. Finally, incident average power is limited when performing nonlinear illumination mode sample excitation in the same way that it is limited in typical linear NSOM experiments. The nanoscopic tip can melt when the taper region of the fiber is thermally heated by more than a few milliwatts.

Collection mode NSOM typically engenders lower background signal levels because the subwavelength probe attenuates the far-field excitation laser intensity (as well as the signal). Also, the nonlinear signal collected by the near-field probe will ultimately exit the fiber optic with a well-defined divergence that is dictated by the numerical aperture of the fiber itself, thus facilitating collection and routing to detectors. Furthermore, arbitrarily high incident laser power can be maintained in collection mode NSOM, as typically the limitation is set by multiphoton ionization damage of the sample, rather than thermal melting of the probe.

When performing collection mode NSOM, it is beneficial to maintain the tip in a fixed tip/laser field geometry and translate the sample in the x , y , and z (feedback) directions. This helps to keep background signals constant throughout a scan, and

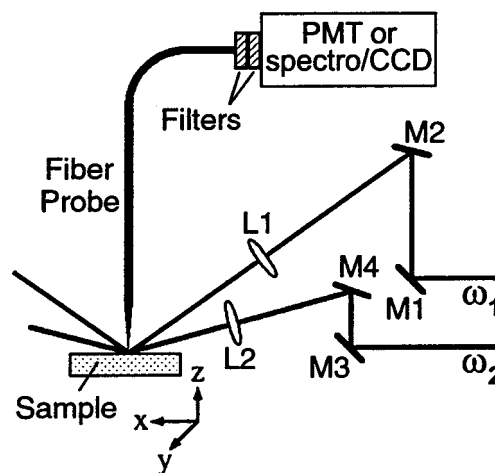


Figure 1. NCIN setup. Steering mirrors (M1–M4), 15 cm focal length fused silica lens (L1), and 8 cm focal length CaF_2 lens (L2). Here shown in the configuration of SFG using frequencies ω_1 and ω_2 , signals generated in the sample were collected by the NSOM fiber probe and directed to a photodetector: either to filters and a Hamamatsu R3896 PMT for imaging, or a 0.3 m spectrograph and nitrogen-cooled CCD (Roper Scientific) to generate spectra. Sample stage piezos performed the x , y , and z directions of motion for both scanning and near-field feedback so that the NSOM probe experiences invariant tip/field geometry. Shear force feedback was utilized to maintain the tip-to-sample distance near ~ 5 nm. All images are 200×200 pixel x , y -arrays and have not been processed.

prevents artifactual contrast that can be generated from spatially inhomogeneous laser pulses. Metal coated NSOM probes, which are a requirement for high spatial resolution and contrast in linear illumination mode NSOM experiments, are not used in the majority of nonlinear collection mode experiments because metals are highly polarizable and can produce nonlinear signals which are stronger than those of less polarizable semiconductor and insulating samples.^{31,37,69} Sharp, metallized tips may also induce significant perturbations to the optical processes in a sample,^{70–72} which is an effect that is exploited in apertureless near-field methods.^{73–77} While the primary focus of our work is on chemical and environmental selectivity in microscopy, we note that we routinely observe sub-diffraction optical spatial resolution in NCIN.

Many variations on our NCIN approach are possible. We currently employ a Thermomicroscopes Lumina system that incorporates a stage scanner with $50 \mu\text{m} \times 50 \mu\text{m}$ horizontal (x – y) and $10 \mu\text{m}$ vertical (z) scan range. It also features a nonoptical, shear-force feedback mechanism that can maintain a constant sample-tip separation near 5 nm.^{78,79} As shown in Figure 1, laser pulses were focused from the far-field to a $\sim (100 \mu\text{m})^2$ spot onto the region of a sample that was investigated by the near-field probe. Signals collected in the near-field were directed by the fiber optic to filters and either a 0.3 m spectrograph and CCD for spectra or a photomultiplier tube (PMT) for imaging. Topographical and optical signals were obtained simultaneously in each experiment for comparison. Forward and backward scans along the same area were collected to produce separate images as a measure of reproducibility. Repeatable optical images could then be added together to reduce random noise. All images in this work are 200×200 pixel arrays, required typically 30–35 min to collect, and have not been processed in any way.

The light source for all of our NCIN experiments consists of a home-built titanium:sapphire (Ti:S) oscillator (800 nm, 480 mW, 30 fs, 88 MHz) which is used to seed a commercial (Spectra-Physics) chirped pulse amplifier (800 nm, 2.25 W, 80

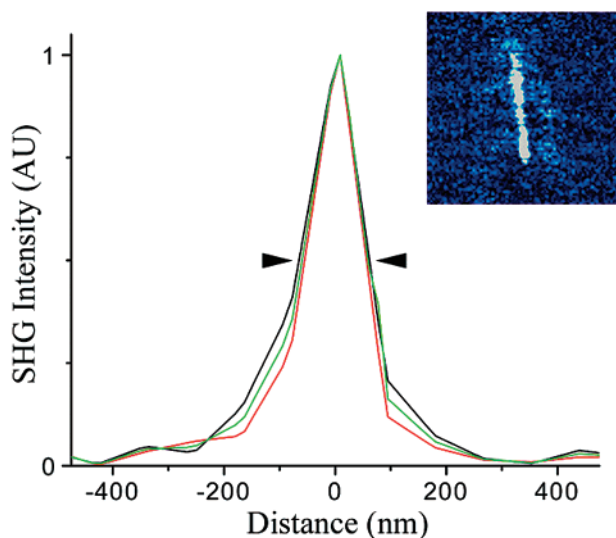


Figure 2. Spatial resolution of SHG NSOM. Three adjacent cross-sectional line traces through an SHG NSOM image produced at $2\omega = 400$ nm (inset) of a $4\ \mu\text{m}$ by $90\ \text{nm}$ single ZnO nanowire show reproducible optical spatial resolution of $\sim 108\ \text{nm}$ (fwhm).

fs, 1 kHz). This output is beamsplit 90:10 using the 90% beam to pump a commercial (Quantronix, Topaz) superfluorescence optical parametric amplifier (OPA) ($1.16\text{--}2.7\ \mu\text{m}$, $300\ \mu\text{J}$ at $1.35\ \mu\text{m}$, 80 fs). Tunable mid-IR wavelengths can be produced via difference frequency generation between the signal and idler OPA wavelengths in a AgGaS crystal ($2.8\text{--}10\ \mu\text{m}$, $20\ \mu\text{J}$ at $4.4\ \mu\text{m}$, 155 fs). The residual 10% of the amplifier output can also be attenuated and used in SFG experiments. Previously, as in the following SHG and THG measurements, we utilized adiabatically pulled fiber optic probes; however, in more recent measurements we have begun to employ chemically etched probes due to the $\sim 10\times$ higher signal levels we have observed as well as the ability to reduce incident laser power levels at the sample.

III. NCIN Performance

To demonstrate the spatial resolution currently achievable with our NCIN system, multiple line traces through an SHG NSOM image of a single ZnO nanowire ($4\ \mu\text{m}$ in length and $90\ \text{nm}$ in diameter) on a sapphire substrate are shown in Figure 2. ZnO nanowires provide a good test of NCIN spatial resolution due to their well-defined size⁸⁰ and strong nonresonant SHG signals which results in good signal-to-noise ratios (here $\sim 30:1$).⁸¹ Furthermore, the near 1-D shape of nanowires offers an approximate optical point source in the direction across their diameter and a test of reproducibility along their length. The reproducible optical spatial resolution for this measurement is $\sim 108\ \text{nm}$ fwhm. We emphasize, however, that NSOM optical resolution, as discussed in detail by Paesler and Moyer,²⁹ is always dependent upon the exact characteristics of the particular tip utilized and the properties of the sample that is examined in a particular experiment. For this reason, a point spread function (and thus an optical transfer function) for this type of microscopy is not a constant of the system as often can be assumed for far-field microscopy techniques.⁸²

It is also important to point out that NSOM experiments have been plagued by artifacts in optical contrast, often believed to result from topographical coupling of optical signals, as discussed by Hecht.⁸³ The theory of near-field optics has not yet been developed sufficiently well to enable the reliable a priori calculation of expected optical responses for an arbitrary

sample or optical process. Therefore, one must resort to empirical methods in order to distinguish genuine image contrast that results from high spatial frequency information in a sample from possible artificial contrast. Hecht concludes that optical contrast in NSOM imaging can be deemed reliable when it does not appear similar to topographical images produced from constant tip-to-sample gap mode measurements (which entails the feedback mechanism utilized in this work and which is the mechanism generally of choice for topographical imaging of soft samples). While this dissimilarity criterion is sensible for many samples, the complex structures contained in many samples which we intend to image (e.g., subcellular structures in cells which are not observable in topographical imaging), we believe that a spectroscopic criterion provides a more convincing method of distinguishing artifactual contrast from genuine information content in the images. Specifically, we resort to comparison of images produced on- and off-resonance in coherent nonlinear optical methods. For example, in the case of THG NSOM imaging of human red blood cells presented below, high optical contrast is observed only in the resonant case (and nonresonant THG signal levels are nonzero).

Finally, while we certainly would not yet characterize the NCIN technique as having “high sensitivity” in terms of the efficiency of converting excitation photons into collected signal photons due to the inefficiency of both nonlinear optical processes and the signal attenuation engendered by the sub-wavelength dimension probe, we believe the technique is potentially very powerful in its applicability to a wide variety of samples. Some examples follow.

IV. Second Harmonic Generation NSOM

SHG imaging has been applied successfully to a variety of chemical problems in far-field studies ranging from materials^{8,10,13} to biological samples.^{9,11,12} Of these, biological samples present the most difficulty due to weaker nonlinear responses as well as higher inherent fragility and disorder. Near-field detected SHG, likewise, has been applied to several types of samples, ranging from metal films³⁷ and piezoceramics⁴³ to Langmuir–Blodgett films⁴¹ and subcellular organelle features.³⁴

The first demonstration of coupling coherent nonlinear optics with NSOM was performed by Smolyaninov et al. on an evaporated silver film in a collection mode geometry using a 20 Hz, 20 ns, Nd:YAG laser at 1064 nm as the excitation source.³⁷ In these initial experiments, they were able to measure spatial variation of SHG signals as a function of surface roughness, correlating local surface topography and *s*- or *p*-incident excitation light with SHG efficiency. Since then, Smolyaninov and other researchers have begun to utilize shorter pulsewidths to increase signal levels and reduce incident average power on the sample. Bozhevolnyi et al. demonstrated illumination mode SHG NSOM on a Langmuir–Blodgett film of 2-docosylamino-5-nitropyridine, a highly nonlinear organic material, using a 80 MHz, 200 fs, Ti:S oscillator as a near-IR tunable light source ($730\text{--}880\ \text{nm}$)⁴¹ and observed efficient SHG from small, isolated domains present in the films. Additionally, due to the tunability of the light source, they were able to observe size effects on SHG efficiency, as larger domain sizes exhibited increased SHG efficiency at longer wavelengths.

In our initial study of SHG NSOM on a biological sample, we explored the use of nonlinear optics as a noninvasive tool to study subcellular features,³⁴ demonstrating chemically selective imaging via selective resonant enhancement of SHG for the first time in NCIN imaging. In these experiments, the results of which are shown in Figure 3, we repeatedly imaged the same

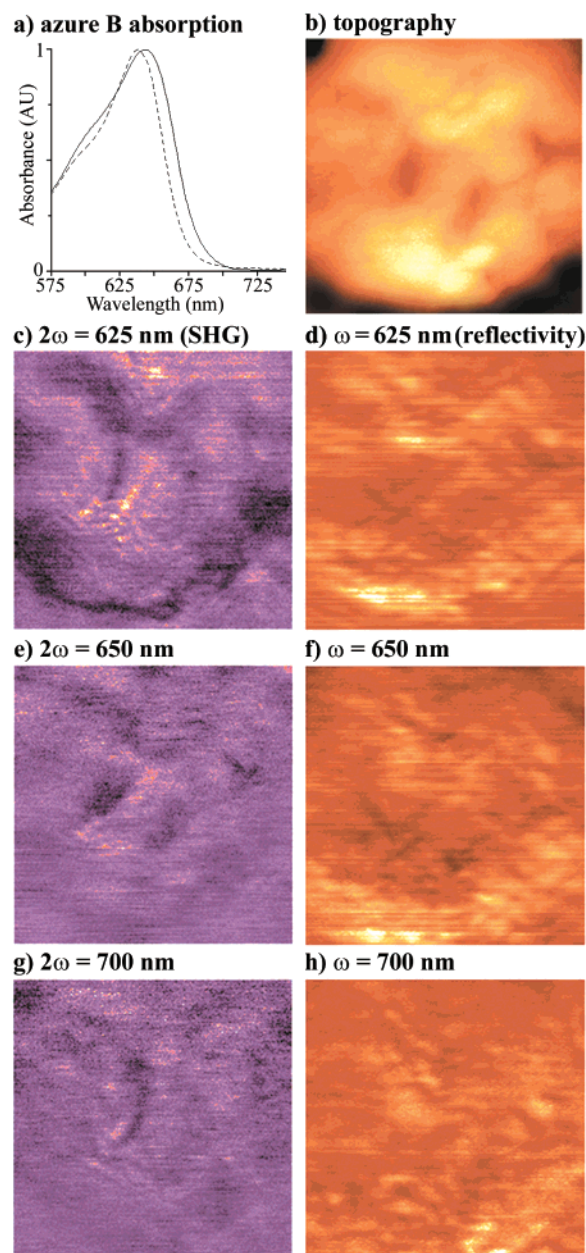


Figure 3. SHG NSOM of NK cells. (a) Linear absorption spectra of the granule specific dye, azure B, a solvatochromic phenothiazine dye,¹³² dissolved in water (solid), and a 50:50 v:v mixture of acetone:hexanes (dashed). (c–h) SHG and linear reflectivity images produced at the detected wavelengths of 625, 650 and 700 nm for the same topographical region of an azure B stained NK cell shown in part b. Field of view is $(10\ \mu\text{m})^2$, maximum topographical height of part b is $1.44\ \mu\text{m}$, each SHG image pixel z -value represents the average of 40 laser shots, incident laser pulse energy was $\sim 5\ \mu\text{J}$, and dark areas in SHG images correspond to low signal (~ 0 photons/laser shot) while bright areas correspond to high signal (~ 3 photons/laser shot). Linear images produced for the same wavelengths as the detected SHG do not resemble the SHG images indicating that second-order polarizabilities are the main source of contrast rather than Fresnel factors. The lower observed SHG contrast at $2\omega = 650$ nm than at $2\omega = 625$ nm indicates a shift of the resonance of the azure B stain to higher frequencies (solvatochromic behavior as shown in part a) and is the result of the low polarity granular membrane environment in which the stain is located. Very little contrast is observed in part g ($2\omega = 700$ nm) due to a loss of enhancement from the azure B. Assignment of the small (~ 300 nm diameter), spherical features observed in part c ($2\omega = 625$ nm) to cytolytic granules was confirmed by confocal fluorescence microscopy, and control experiments conducted on unstained NK cells did not exhibit these features (not shown).

area of a natural killer (NK) cell and stepped the wavelength of our amplified, tunable femtosecond laser such that SHG frequencies became resonant with the absorption spectrum of an organelle-specific stain, azure B. SHG images produced with the incident laser tuned to an azure B electronic transition resulted in resonant enhancement of the SHG from only those spatial regions of the NK cell containing cytolytic granules. Furthermore, the highest SHG contrast, i.e., the largest resonant enhancement, shown in part c, was observed at bluer wavelengths than the linear absorption λ_{max} of azure B produced with water as the solvent. Because the dye exhibits a solvatochromic shift to the blue in lower polarity environments as we have shown in part a, we believe that interfacial selectivity was observed in these measurements, the low polarity environment being provided by the granular membrane. Linear reflectivity images produced at the same wavelengths as the detected SHG do not bear semblance to the SHG images which indicates that the SHG contrast does not result from spatial variation of Fresnel factors.

In our SHG NSOM experiments, chemically selective contrast is demonstrated, however, we achieved this by utilizing a foreign stain introduced into the cell for the same purpose as for fluorescence labeling experiments. While this method constitutes a new approach to dye labeling obviating the requirement of the dye being photoemissive and with the prospect of membrane sensitivity, it does not directly exploit intrinsic chromophores of the sample itself. A general problem with SHG probing of biological samples is the lack of chromophores having transition frequencies in the visible region of the spectrum, where SHG is most practical. A region of the spectrum wherein all biological samples have intrinsic chromophores is the mid-infrared, and the most frequently practiced nonlinear optical spectroscopy technique that gains access to this region of the spectrum is SFG.

V. Sum Frequency Generation NSOM

SFG microscopy is similar in principle to SHG microscopy, although in practice, it is significantly more difficult. The interest in SFG microscopy is primarily due to the chemical information which becomes obtainable from molecules explicitly residing at interfaces via their vibrations.³¹ It is important to note that there is rapid ongoing progress in the development of linear-IR NSOM.^{84–92} These linear-IR studies, however, suffer from high background signals, low contrast, problems with topographical artifacts, and have intrinsic bulk sensitivity. Also, progress in coupling Raman spectroscopy with NSOM has been made,^{93–104} but this technique, which also inherently exhibits bulk sensitivity, does not yet lend itself to a broad range of samples. SFG has only recently begun to be exploited as a contrast mechanism in microscopy. The first far-field example did not appear until the work of Florsheimer et al. in 1999.¹⁴ Far-field SFG microscopy suffers from spatial resolution that is limited by diffraction of the shorter wavelength of the two incident beams (as the SFG is only produced from the region of spatial overlap of the input pulses used in the process). Moreover, due to phase matching conditions, the SFG signal will change laboratory coordinates as the wavelength of either incident laser pulse is changed, unless the input beams are made to be collinear, and the very high quality optics required for this configuration are currently not available. These problems are transcended when SFG signals are collected in the near-zone due to probe-limited spatial resolution and intrinsic relaxation of phase matching conditions.

Concurrently, our group³⁵ and Shen et al.⁵⁶ demonstrated SFG near-field imaging techniques using two very different ap-

proaches. The approach of Shen et al. involved mixing the fundamental (1047 nm) and frequency doubled (523.5 nm) outputs of a 10 ns, Q-switched Nd:YLF laser in crystalline nitrophenylprolinol samples, an organic nonlinear material, to produce the sum frequency (349 nm).⁵⁶ A PSTM near-field configuration was utilized which requires the sample to be directly deposited on a prism. From these measurements, they observe a defect in one of the imaged crystals signified by a decrease in second-order signal levels from an otherwise homogeneous spatial distribution of signal from the nonlinear crystal. However, the experimental wavelengths utilized did not allow for vibrational analysis of the sample.

In our approach to near-field SFG imaging, we summed pulses of 800 nm light with tunable mid-IR pulses generated with an amplified, femtosecond Ti:S laser to produce SFG around 620–710 nm.³⁵ The SFG was detected in oblique collection mode geometry from chemical vapor deposited (CVD) disks of ZnSe, a wide band gap semiconductor (2.8 eV at 300 K)¹⁰⁵ that, like nitrophenylprolinol crystals, lacks inversion symmetry and typically results in a large bulk signal contribution. As shown in Figure 4, parts a–d, for the topographical region shown in part e, striation patterns were observed in the SFG NSOM images that produce stronger SFG signals than homogeneous regions of the semiconductor. Utilizing the tunability of the IR wavelength in our experiment, we were also able to observe variations in image contrast as a function of IR wavelength. Interestingly, the experimental frequencies utilized in these images do not correspond to vibrational frequencies of the bulk sample. Only one, 6-fold degenerate component of the second-order response exists for crystals of the zincblende structure: $\chi^{(2)}_{xyz} = \chi^{(2)}_{xzy} = \chi^{(2)}_{yxz} = \chi^{(2)}_{yzx} = \chi^{(2)}_{zxy} = \chi^{(2)}_{zyx}$.¹⁰⁶ Variation of the incident laser polarization showed the second-order sample response to be anisotropic whereas the bulk crystal response is isotropic, indicating deviation from zincblende symmetry. We have confirmed that these striation patterns ultimately result from defects or impurities in the sample, and not from an optical interference artifact, as such patterns were not observed for adjacent regions (10 μm away) of the sample that were imaged using the exact same laser alignment, and variation of the incident laser polarization and IR wavelength did not change the striation pattern. Similar results on ZnSe samples have also been observed by Hocker et al. using crossed-polarizer microscopy,¹⁰⁷ although those results were on a 10–100 times larger scale. Other work has indicated that striation features due to glide plane formation may be a crystal strain relief mechanism common to many II–VI materials as a result of impurities.^{108,109} We hope to elucidate the chemical composition of these features. For that reason, we perform SHG as well as the MSFG NSOM experiments described below.

The contrast in our SFG NSOM images can result from variations in either nonresonant or resonant components of the second-order nonlinear susceptibility tensor. However, nonresonant SFG is unlikely to produce optical contrast that varies as the wavelength of the IR pulse is scanned over small ranges, since it should be approximately wavelength independent. Conversely, resonant enhancement effects can produce dramatic variations (by up to 10^4) in SFG signals with small changes in the IR frequency.³¹ The source of resonant enhancements in a semiconductor, however, can be difficult to determine, as many types of defect levels may exist within the band gap region, which can also be dependent on exact sample preparation methods.^{108,109} Energy levels may arise from interfacial effects such as intraband energy levels produced from the sharp change in band structure near an interface as well as dangling bonds

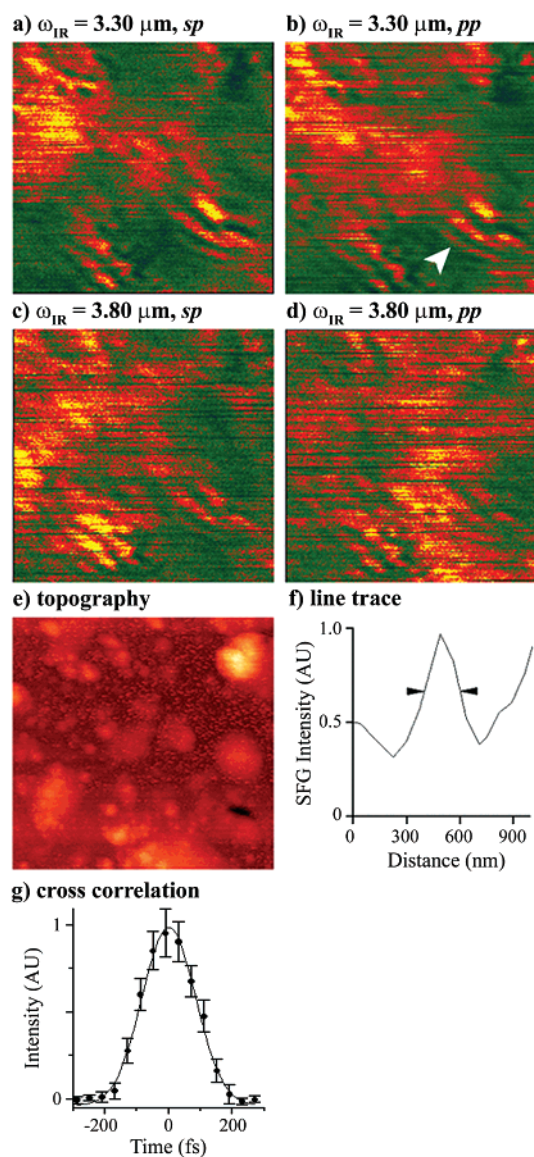


Figure 4. SFG NSOM of CVD ZnSe. (a–d) SFG images of a (10 μm)² area of CVD ZnSe, shown topographically in part e, generated by summing 800 nm pulses with pulses of the indicated IR wavelengths and respective polarization combinations. The maximum topographical height of part e is 78 nm, each optical pixel z-value represents the average of 40 laser shots, incident laser pulse energies were $\sim 3 \mu\text{J}$ of 800 nm and $\sim 10 \mu\text{J}$ of IR, dark areas of the SFG images correspond to low signal (~ 0 –1 photon/laser shot) and bright areas correspond to high signal (~ 5 photons/laser shot). The SFG images exhibit a dependence on both the IR wavelength and the incident polarization of the 800 nm pulses. The polarization state of the detected SFG signals was not resolved. Parallel features in the SFG images are observable, which were experimentally determined not to result from interference effects. These features exhibit stronger SFG than homogeneous regions of the semiconductor and are interpreted to result from strain within the ZnSe crystal lattice formed in regions of high impurity concentration.¹⁰⁷ The spatial variation of the optical signals is also clearly observed to vary when the 800 nm light polarization is rotated and/or the IR wavelength is changed. Variation of the SFG images with incident laser polarization is indicative of anisotropic components of the sample response whereas the bulk crystal response is isotropic.¹⁰⁶ The white arrow drawn in part b indicates the (111) crystal direction (based upon the work of Hocker et al.)¹⁰⁷ as well as the region shown in part f used to determine the spatial resolution, which is ~ 190 nm. (g) Near-field temporal cross-correlation measurements were performed to confirm that detected signals resulted from the SFG process. Each point in the plot represents the average of 15,000 laser shots and RMS noise values are displayed. As can be seen, signals were only detected when the two pulses used in the experiment were temporally overlapped.

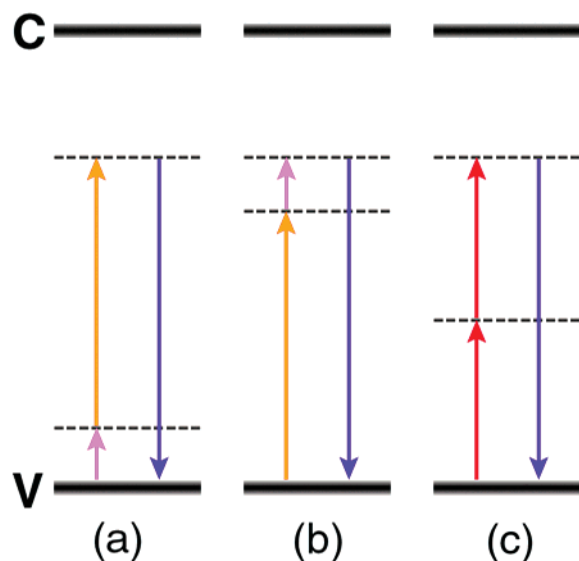


Figure 5. Second-order nonlinear mixing schemes. The origin of resonant enhancements in ZnSe can be discerned by exploring different second-order mixing schemes. Three schemes are possible: (a) SFG involving an initial interaction with an IR photon followed by the pump photon, (b) SFG with the IR and pump photon order reversed exploring a different intermediate state but the same two-photon state, and (c) SHG involving two degenerate photons mixing via yet another intermediate state but having the same two-photon state as both possible SFG processes. It should be noted that both SFG processes are allowed to occur; however, process would access the same one-photon level consistently throughout all of the SFG images in Figure 6 and not produce variation in image contrast when the IR wavelength is changed. If SFG and SHG experiments with degenerate two-photon states are compared and appear similar, resonant enhancement at the two-photon level is likely, but if they appear dissimilar, one-photon resonance enhancements (which are not degenerate for the two experiments) are likely. The valence (v) and conduction (c) edges of ZnSe are also indicated (to scale).

which terminate the crystal. Additional levels can occur due to bulk material imperfections such as lattice defects and chemical impurities such as starting materials, hydrocarbons, and oxides.

Assuming that resonant enhancement of the SFG is the operative contrast mechanism in this sample, a scheme to discriminate whether resonant enhancements are generated from one- or two-photon energies is to measure SHG and SFG signals from the same sample area. As illustrated in Figure 5, parts a–c, SFG and SHG experiments can be designed to have degenerate two-photon energies but nondegenerate one-photon energies. Similar images produced by the two techniques having the same two-photon energy would provide evidence that the two-photon state is responsible for resonantly enhanced optical contrast, while differences between the SFG and SHG images would indicate one-photon resonant enhancement.

Results of SFG and SHG NSOM measurements designed to have degenerate two-photon energies are shown in Figure 6, parts a–h, for the same topographical region shown in part i. Except for a large round feature seen in parts d and f, which seems to be anticorrelated with the SFG images, the SHG NSOM images appear featureless, indicating that neither the one- nor two-photon energies levels of the SHG mixing process shown in Figure 5, part c, gives rise to resonance conditions in the SHG images. It can also be concluded that contrast between the SFG NSOM images is not being generated from the one-photon energy level involved in the SFG mixing process shown in Figure 5, part b, (the 800 nm photon) as this energy level is a constant throughout each of the presented SFG NSOM images. Therefore, one-photon energy levels of the SFG mixing process

shown in Figure 5, part a, are likely to be the source of the SFG image contrast. These results support the idea that molecular vibrations and semiconductor defect levels are being probed in the SFG NSOM measurements. Comparison of the experimental IR and SF energies with defect energy measurements obtained by capacitance techniques, however, is difficult due to large variation in reported values and assignments.^{108,110,111} These disparities may result from details of sample preparation methods, the precision of the different techniques employed, and variation in semiconductor models.

VI. Third Harmonic Generation NSOM

Third-order nonlinear optical probes, such as THG, which can be produced efficiently from both isotropic and anisotropic sample environments, in distinction from second-order measurements, can provide complementary environmental selectivity in high spatial resolution imaging. Nonresonant THG is developing rapidly as a far-field imaging technique. Much of the interest has been due to the results of Tsang¹⁵ who first reported what is now often referred to as “surface” THG, viz. very tightly focused, high intensity (100s of GW/cm²) laser pulses can produce THG signals that are several orders of magnitude ($\sim 10^5$) stronger when the focal volume of the laser contains an interfacial region such as air/glass. This result, which is emerging to be a generally observable effect in the far-field nonresonant case, appears to be in stark contrast to the generally accepted view of THG as a bulk probe. The mechanism of this apparent “surface” THG has been proposed to either embody an enhanced surface component of a material’s $\chi^{(3)}$ response, which would imply monolayer sensitivity, or may be described by the classically calculated THG efficiency of tightly focused Gaussian beams in a region where either a change in refractive index, n , or $\chi^{(3)}$ exists as first purported by Boyd.³² The latter of these possible mechanisms, which would involve thousands of monolayers and, therefore, constitute a bulk measurement, implies that a change in either n or $\chi^{(3)}$ would assist in relaxing the phase matching condition for the process, resulting in a very significant increase in THG efficiency. In any case, far-field, nonresonant THG has been successfully applied by several researchers to image a variety of samples.^{15–20}

To explore the utility of THG as a contrast mechanism in near-field imaging, we performed NSOM-detected THG experiments on samples of human erythrocytes and tuned our excitation laser on and off resonance with the absorption spectrum of oxyhemoglobin (oxyHG) ($\lambda_{\text{max}} = 415$ nm), a nonfluorescent, bulk chromophore that is free in the cytosol.³⁶ These experiments probe the utility of THG as a chemically specific optical contrast mechanism, and in the nonresonant case, serve as a test of the two aforementioned proposed sources of far-field, nonresonant THG “surface” enhancement due to the a priori relaxation of phase matching conditions inherent in NCIN. Moreover, they demonstrate the use of intrinsic chromophores for chemically selective imaging.

THG NSOM images of erythrocytes produced at $3\omega = 420$ and 490 nm are shown in Figure 7, parts a and b, respectively, for the same topographic region shown in part c.³⁶ As can be clearly discerned in these images, high contrast is observable in part a, in which the third harmonic is resonant with the strong Soret absorption band of oxyHG as shown in d. While THG signal levels are nonzero in b in which the third harmonic is not resonant with the electronic absorption band of the chromophore, optical contrast between the fused silica substrate and the erythrocytes is not observed. Figure 7, part e, displays the cubic dependence of signal levels collected at the THG

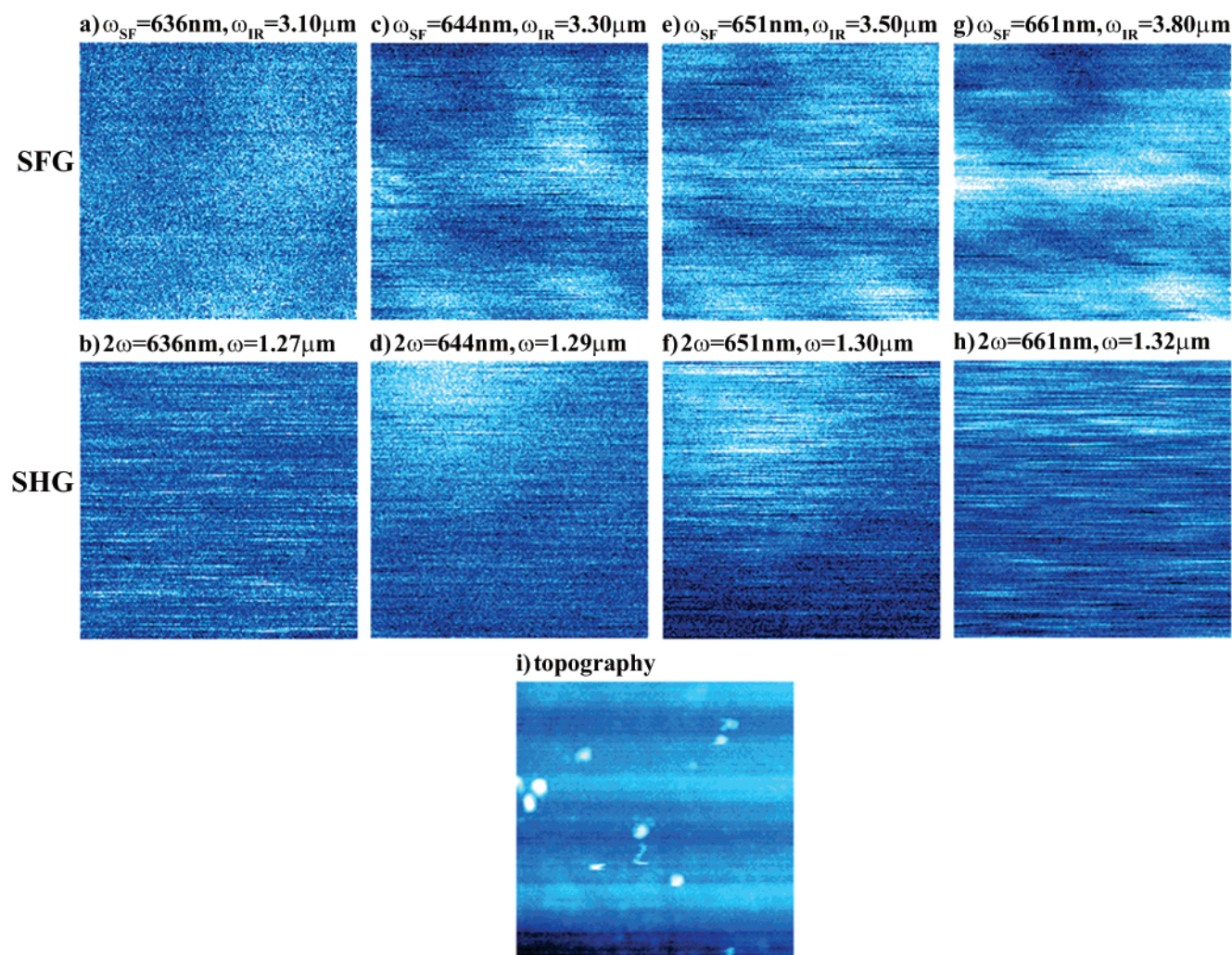


Figure 6. SFG and SHG NSOM of CVD ZnSe. To determine the origin of resonant enhancements in SFG NSOM images of CVD ZnSe, SFG (upper row), and SHG NSOM images (lower row) were produced at the same detected two-photon energy, shown in parts a–h, for the same $(10\ \mu\text{m})^2$ topographical region shown in i. All SFG images were produced with the 800 nm photons and the indicated IR wavelength. All optical images were produced using vertically polarized laser pulses. Aside from a large round feature in the parts d and f of the SHG images, which appears to be anti-correlated with the SFG images (bright in the SHG and dark in the SFG measurements), the SFG and SHG images do not resemble each other. The lack of similarity between two-photon degenerate SHG and SFG images indicates that one-photon resonances are the likely source of the optical contrast in the SFG images. Furthermore, variation in contrast exists between the SFG NSOM images produced at different IR wavelengths. Therefore, the source of IR wavelength dependent contrast in the SFG NSOM images can be assigned to resonant enhancement from one-photon energy levels that correspond to IR wavelengths as in the mixing process shown in Figure 5, part a. It is worth noting that a one-photon resonance with the 800 nm pulses, the mixing scheme shown in Figure 5b, would be a constant source of contrast throughout the SFG image series, and does not appear to be important in these measurements. Dark regions of optical images correspond to low signals (~ 0 –1 photon/shot), bright areas correspond to high signals (~ 4 photons/shot), each optical pixel z-value represents the average of 40 laser shots, incident laser pulse energies were $\sim 3\ \mu\text{J}$ of 800 nm and $\sim 10\ \mu\text{J}$ of IR, and the maximum topographic height of part a is 155 nm.

frequency on incident laser power, which confirms that the signals result from the THG process. Upon the bases of these results, it appears that THG can indeed produce chemically specific image contrast with bulk environmental selectivity using resonant enhancement from intrinsic chromophores. The lack of optical contrast between the amorphous glass substrate and the erythrocyte in the nonresonant THG NSOM image (Figure 7, part b) indicates that far-field “surface” selective THG signals actually result from a relaxation of phase matching conditions at interfaces and not from intrinsic surface components of the $\chi^{(3)}$ response. Surface components of the $\chi^{(3)}$ response would be expected to be quite different for amorphous glass and the organic membrane of a cell and, therefore, should have resulted in nonresonant THG contrast in similarity to far-field THG imaging results if such components were significant. This, as explained above, implies that far-field THG imaging constitutes a bulk spectroscopic probe.

VII. Multiplex Sum Frequency Generation NSOM

Increased spectral resolution allows for more exact analysis of sample chemical composition as well as more specific chemical contrast in NCIN imaging. The spectral resolution that we have demonstrated previously using a femtosecond light source ($\sim 200\ \text{cm}^{-1}$) is sufficient for the analysis of electronic transitions in many samples; however, this energy resolution is clearly insufficient for detailed vibrational analysis wherein transitions are narrow ($\sim 10\ \text{cm}^{-1}$) in width and in which multiple vibrational bands can be closely spaced. However, a variety of far-field techniques, which we are now exploring, can be applied to this problem.

The traditional approaches of picosecond and nanosecond far-field SFG spectroscopy, which have been successfully been applied to many chemical problems,^{63,112–118} are not broadly applicable to typical samples in NSOM imaging due to the high

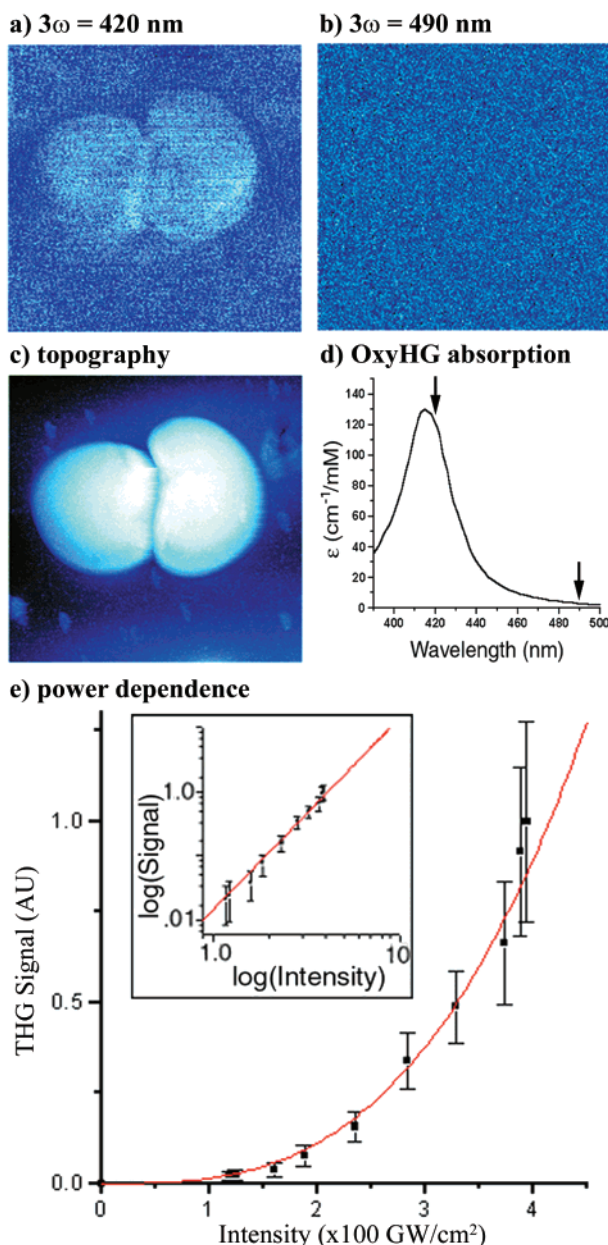


Figure 7. THG NSOM of human erythrocytes. (a,b) THG NSOM images of two coagulated human erythrocytes in a $(17\ \mu\text{m})^2$ area produced at $3\omega = 420$ and 490 nm, respectively for the same area shown topographically in c. The maximum topographic height of c is 710 nm, optical pixel z -values represent the average of 40 laser shots, incident laser pulse energy was $\sim 15\ \mu\text{J}$, dark regions correspond to low signals (~ 0 to 1 photon/laser shot) and bright regions correspond to high signals (~ 3 photons/laser shot). As indicated by the linear absorption spectrum shown in d,¹³³ THG contrast is very high in part a when 3ω is resonant with the Soret transition of oxyHG and no contrast is observed in part b when the THG is nonresonant. OxyHG, a nonfluorescent, intrinsic chromophore, is a protein that is free in the cytosol, indicating that bulk environmental selectivity is observed, and therefore, resolution-limited features do not appear in part a. The lack of optical contrast in part b (the nonresonant THG measurement) provides evidence that far-field nonresonant THG measurements, which are debated to exhibit surface selectivity, actually constitute a bulk probe. (d) The power dependence of the collected signal through the NSOM fiber probe was measured at $3\omega = 420$ nm. A fit to the data points, each point representing the average of 21,000 laser shots (RMS noise values shown), shows a third order power dependence with fundamental intensity. The data represented logarithmically in the inset shows a slope equal to three linear fit to the data, confirming that detected signals result from the THG process. Near-field detected spectra also confirmed this finding (not shown).³⁶

peak power required to generate detectable near-field signal levels, and the generally low damage threshold of many samples. Two techniques incorporating femtosecond pulses, and thus reduced average power, are of potential utility. McGuire et al. demonstrated a Fourier transform interferometric SFG technique using two femtosecond pulses, one visible and one IR, to produce high resolution ($\sim 6.6\ \text{cm}^{-1}$) far-field SFG spectra.¹¹⁹ This method has the clear advantages of very high peak power with a minimum of average power as well as spectral resolution determined by the step size of the interferometer. Also, Richter et al. were the first to demonstrate so-called “broad-bandwidth” SFG by masking one femtosecond pulse of spectral bandwidth to produce a narrow-bandwidth ($\sim 4.8\ \text{cm}^{-1}$), picosecond pulse, which was then summed with a broad-bandwidth femtosecond pulse.¹²⁰ The output is energy resolved with a spectrograph and array detection to produce SFG spectra with spectral resolution determined by the narrow band pulse and spectral coverage determined by the femtosecond pulse ($> 250\ \text{cm}^{-1}$). Already, this important nonlinear technique, which has more clearly been referred to as “multiplex” SFG recently,¹²¹ is being utilized in many studies.^{121–126}

We have recently explored near-field detected MSFG imaging using a simplified setup as compared to that of Richter. Rather than spectrally dispersing a pulse, masking its bandwidth, and temporally recompressing it to produce a narrowband pulse, we have simply incorporated a very narrow ($\sim 15\ \text{cm}^{-1}$ fwhm, 790.0 nm), single cavity, band-pass filter into our previous SFG NSOM setup. We demonstrate in Figure 8, part a, that this filter converts an 80 fs pulse into a 1.6 picosecond pulse, deviating from a Gaussian temporal profile only at times later than the maximum pulse intensity which is utilized in the experiment. MSFG signals collected by the near-field probe can be directed to a 0.3 m spectrograph and integrated on a CCD camera to produce MSFG spectra.

MSFG NSOM images produced by collecting all of the bandwidth of the SFG signals are shown in Figure 8, part c, for the topographical region shown in b. Spatially resolved MSFG spectra were then acquired for the labeled regions in part c and are shown in part d. These MSFG NSOM spectra, which exhibit more than $200\ \text{cm}^{-1}$ of spectral coverage due to the bandwidth of the IR pulse, were typical of the bright and dark regions present in the image. The observed spectral resolution ($\sim 18\ \text{cm}^{-1}$) appears to be similar to that of the bandwidth of the narrow band filter. While we are tentative about the assignments of the peaks observed in the spectra, we note their proximity to known H–Se bond frequencies (we observe a peak at $2360\ \text{cm}^{-1}$, compared to reported H_2Se literature values near $2357\ \text{cm}^{-1}$).¹²⁷ H_2Se is a starting material for the CVD process and therefore, H–Se type bonds may be prevalent in materials produced by this method though investigation of more spectral regions is required to confirm this possibility.¹²⁸ Furthermore, higher spectral resolution can be provided in this experimental technique simply by incorporating a filter of narrower bandwidth and increased spectral coverage can be produced by incorporating shorter IR pulsewidths.

A significant complication that affects MSFG in general is that atmospheric absorptions, especially water and CO_2 , can produce structure in the IR pulse that, subsequently, will appear in the energy resolved SFG spectrum. We point out that such spectral artifacts, if they were present in the spectral region investigated in Figure 8, would appear in all spectra acquired from any region of the sample. Because the spectral absorptions occurring in the atmosphere are a constant, such artifacts cannot

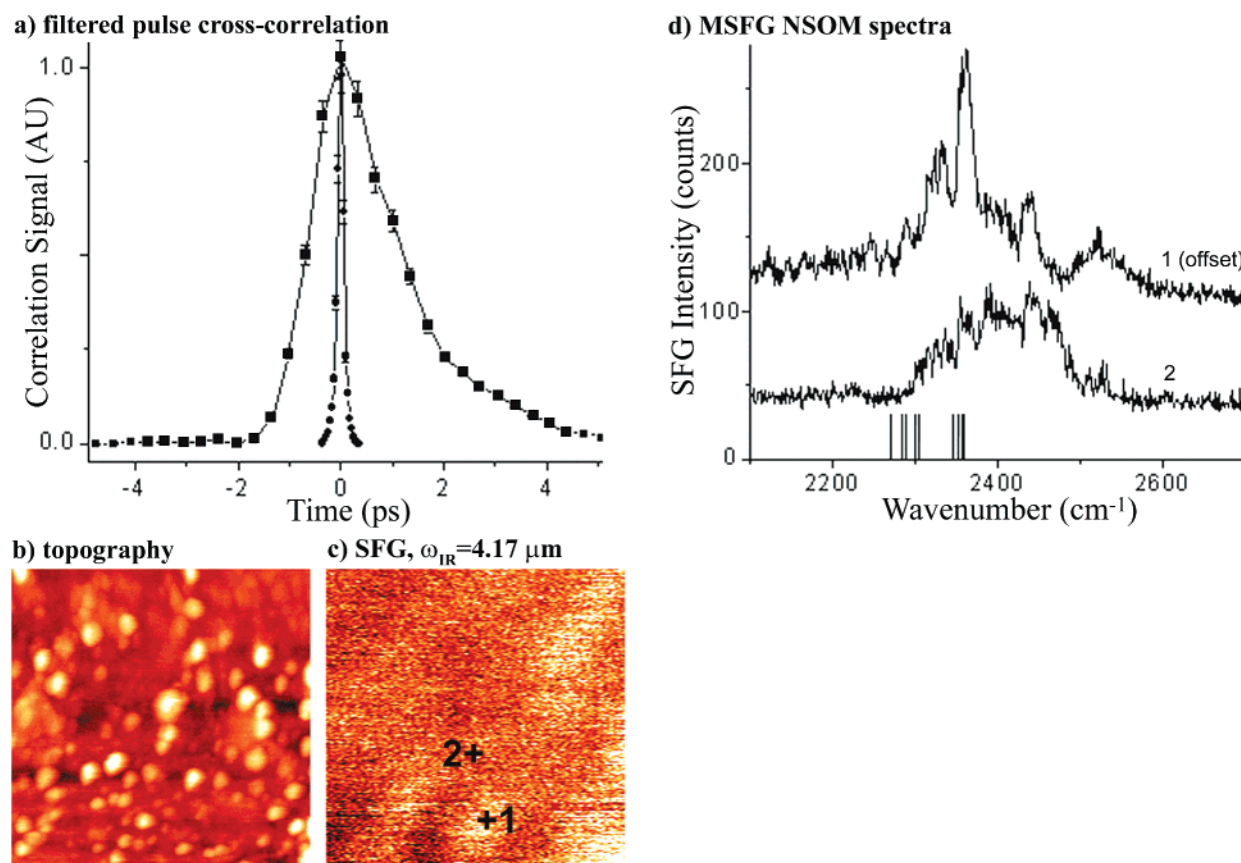


Figure 8. MSFG NSOM of CVD ZnSe. (a) Far-field temporal correlation measurements (produced in the far-field with a KDP crystal) of an 800 nm, 80 fs pulse with itself (circles) and with the same 800 nm, 80 fs pulse after it has been spectrally filtered to produce a narrow bandwidth pulse (790.0 nm center wavelength, $\text{fwhm} = 15 \text{ cm}^{-1}$) (squares). Each point represents the average of 15,000 laser shots and RMS noise values are shown. The narrowband pulse exhibits a Gaussian temporal profile except for a low intensity tail to later time. Neglecting the low intensity tail, which is not used in the mixing process, the Gaussian portion of the pulse exhibits a fwhm of $\sim 1.6 \text{ ps}$. Near-field detected SFG signals were produced by summing the narrowband 790.0 nm pulses with $4.17 \mu\text{m}$, 155 fs pulses on a sample of CVD ZnSe. Incident laser pulse energies were $\sim 2 \mu\text{J}$ at 790.0 nm and $\sim 10 \mu\text{J}$ at $4.17 \mu\text{m}$. Unresolved SFG signals were collected on a PMT to produce SFG NSOM images, shown in part c of the same ($5 \mu\text{m}$)² region of ZnSe shown topographically in part b. The NSOM probe was then held over regions of high and low SFG signal, at locations indicated in part c, and the collected signals were spectrally dispersed with a 1200 gr/mm grating and spectrograph and integrated for 120 s on a liquid nitrogen-cooled CCD. The resulting MSFG spectra, which were typical of the high (~ 4 photons/laser shot) and low signal (~ 0 to 1 photon/laser shot) regions of this particular ZnSe sample, are shown in part d and have been offset for clarity. For SFG-bright regions (such as position 1 in part c), an intense, narrow ($\sim 18 \text{ cm}^{-1}$) peak was consistently observed near 2360 cm^{-1} , similar in energy to transition frequencies of H–Se stretching vibrations that are both Raman and IR active. For comparison, SFG allowed transition frequencies of H_2Se , a starting material for the synthesis of the sample,¹²⁸ for gas, liquid, and solid phases are shown in part d as stick spectra.¹²⁷ Integration of the spectra closely reproduces the observed signal levels for the respective locations of part c. The maximum topographic height of part b is 59 nm and optical pixel z -values in part c represent the average of 50 laser shots.

contribute to the strong peak observed at 2360 cm^{-1} for the bright regions of the SFG NSOM image shown in Figure 8, part c.

VIII. Conclusions and Outlook

We have demonstrated the utility of coherent nonlinear optical spectroscopy for nanoscopic sample imaging with a variety of mixing processes, including SHG, SFG, THG, and MSFG. Resonant enhancement has been demonstrated as a novel contrast mechanism in NSOM imaging that provides chemical selectivity based upon electronic and/or vibrational molecular transitions, while environmental selectivity is achieved via the order of the nonlinear process. We have focused our efforts on biological imaging due to the breadth of potential applications; however, we are finding the extension of these techniques to material science to be quite revealing as well as more straightforward due to higher damage thresholds, higher intrinsic nonlinearity, and reduced sample complexity. For instance, we have recently applied NCIN to the characterization of interchain

species in conjugated polymer films, which we have previously studied in emission,¹²⁹ using THG to spatially map the presence of low energy, nonradiative electronic species that form upon thermal annealing,¹³⁰ an application that is obviously not solvable by fluorescence NSOM.

We have recently reported another manifestation of a novel coherent nonlinear optical process: ultraviolet stimulated emission from individual ZnO nanowires (the same nanowires used as a test of optical resolution I, Figure 2).¹³¹ In these experiments, axially directed photoluminescence (waveguiding) at low optical pump powers as well as stimulated emission at higher pump powers was spectrally resolved and imaged. Due to the directionality of the emission and the observed spectral line widths, we believe that these nanowires behave as active laser cavities wherein the wire ends serve as cavity mirrors. In these measurements, which exhibit a nonlinear dependence of the coherent signals on incident pump power, nanowire stimulated emission properties (i.e., divergence angle, line width, etc.) and possible loss mechanisms can be characterized as a function of

nanowire dimensions and the supporting substrate in order to aid in device design. Furthermore, the high nonlinear harmonic generation efficiency of these materials may be exploited in optical circuits to provide frequency conversion or as an ultrafast switching mechanism.⁸¹

We will continue to apply the NCIN methods discussed in this work to a variety of biological and material science problems, as well as to expand the utility of NCIN by exploring with additional nonlinear optical techniques and time-resolution capabilities. The continuing development of these novel probes which interrogate the chemical properties of a sample on the nanoscale promise to provide a wealth of new information.

Acknowledgment. This work was supported by the Experimental Physical Chemistry Division of the National Science Foundation.

References and Notes

- (1) Lakowicz, J. R. *Topics in Fluorescence Spectroscopy*; Plenum Press: New York, 1991.
- (2) Sabatini, B. L.; Svoboda, K. *Nature* **2000**, 408, 589–93.
- (3) Schwille, P.; Haupts, U.; Maiti, S.; Webb, W. W. *Biophys. J.* **1999**, 77, 2251–65.
- (4) Oheim, M.; Beaupaire, E.; Chaigneau, E.; Mertz, J.; Chrapak, S. *J. Neurol. Methods* **2001**, 111, 29–37.
- (5) Wei, Z.; Wright, J. C. *Phys. Rev. Lett.* **1999**, 83, 1950–3.
- (6) Hochstrasser, R. M. *Chem. Phys.* **2001**, 266, 273–84.
- (7) Yu, J.-Y.; Nagasawa, Y.; van Grondelle, R.; Fleming, G. R. *Chem. Phys. Lett.* **1997**, 280, 404–10.
- (8) Henrichs, S. E.; Sample, J. L.; Shiang, J. J.; Heath, J. R.; Collier, C. P.; Saykally, R. J. *J. Phys. Chem. B* **1999**, 103, 3524–8.
- (9) Lewis, A.; Khachatourians, A.; Treinin, M.; Zhongping, C.; Peleg, G.; Friedman, N.; Bouevitch, O.; Rothman, Z.; Loew, L.; Sheres, M. *Chem. Phys.* **1999**, 245, 133–44.
- (10) Smilowitz, L.; Jia, Q. X.; Yang, X.; Li, D. Q.; McBranch, D.; Buelow, S. J.; Robinson, J. M. *J. Appl. Phys.* **1997**, 81, 2051–4.
- (11) Campagnola, P. J.; Mei-de, W.; Lewis, A.; Loew, L. M. *Biophys. J.* **1999**, 77, 3341–9.
- (12) Moreaux, L.; Sandre, O.; Mertz, J. *J. Opt. Soc. Am. B* **2000**, 17, 1685–94.
- (13) Sun, C. K.; Chu, S.-W.; Tai, S.-P.; Keller, S.; Mishra, U. K.; Denbaars, S. P. *Appl. Phys. Lett.* **2000**, 77, 2331–3.
- (14) Florsheimer, M.; Brillert, C.; Fuchs, H. *Langmuir* **1999**, 15, 5437–9.
- (15) Tsang, T. Y. F. *Phys. Rev. A* **1995**, 52, 4116–25.
- (16) Barad, Y.; Eisenberg, H.; Horowitz, M.; Silberberg, Y. *Appl. Phys. Lett.* **1997**, 70, 922–4.
- (17) Muller, M.; Squier, J.; Wilson, K. R.; Brakenhoff, G. J. *J. Microscopy* **1998**, 191, 266–74.
- (18) Yelin, D.; Silberberg, Y.; Barad, Y.; Patel, J. S. *Appl. Phys. Lett.* **1999**, 74, 3107–9.
- (19) Yelin, D.; Silberberg, Y. *Opt. Express* **1999**, 5.
- (20) Squier, J.; Muller, M. *Rev. Sci. Instrum.* **2001**, 72, 2855–2867.
- (21) Zumbusch, A.; Holtom, G. R.; Xie, X. S. *Phys. Rev. Lett.* **1999**, 82, 4142–4145.
- (22) Muller, M.; Squier, J.; De Lange, C. A.; Brakenhoff, G. J. *J. Microscopy* **2000**, 197, 150–8.
- (23) Hashimoto, M.; Araki, T.; Kawata, S. *Opt. Lett.* **2000**, 25, 1768–70.
- (24) Cheng, J. X.; Volkmer, A.; Book, L. D.; Xie, X. S. *J. Phys. Chem. B* **2001**, 105, 1277–1280.
- (25) Volkmer, A.; Cheng, J. X.; Xie, X. S. *Phys. Rev. Lett.* **2001**, 87, 3901–U47.
- (26) Cheng, J. X.; Book, L. D.; Xie, X. S. *Opt. Lett.* **2001**, 26, 1341–1343.
- (27) Dunn, R. C. *Chem. Rev.* **1999**, 99, 2891–927.
- (28) Hecht, B.; Sick, B.; Wild, U. P.; Deckert, V.; Zenobi, R.; Martin, O. J. F.; Pohl, D. W. *J. Chem. Phys.* **2000**, 112, 7761–74.
- (29) Paesler, M. A.; Moyer, P. J. *Near-field Optics: Theory, Instrumentation, and Applications*; Wiley: New York, 1996.
- (30) Jackson, J. D. *Classical Electrodynamics*, 3rd ed.; Wiley: New York, 1999.
- (31) Shen, Y. R. *The Principles of Nonlinear Optics*; J. Wiley: New York, 1984.
- (32) Boyd, R. W. *Nonlinear Optics*; Academic Press: Boston, 1992.
- (33) Butcher, P. N.; Cotter, D. *The Elements of Nonlinear Optics*; Cambridge University Press: Cambridge, 1990.
- (34) Schaller, R. D.; Roth, C.; Raulet, D. H.; Saykally, R. J. *J. Phys. Chem. B* **2000**, 104, 5217–5220.
- (35) Schaller, R. D.; Saykally, R. J. *Langmuir* **2001**, 17, 2055–2058.
- (36) Schaller, R. D.; Johnson, J. C.; Saykally, R. J. *Anal. Chem.* **2000**, 72, 5361–5364.
- (37) Smolyaninov, I. I.; Zayats, A. V.; Davis, C. C. *Phys. Rev. B* **1997**, 56, 9290–9293.
- (38) Smolyaninov, I. I.; Zayats, A. V.; Davis, C. C. *Opt. Lett.* **1997**, 22, 1592–1594.
- (39) Bozhevolnyi, S. I.; Pedersen, K.; Skettrup, T.; Zhang, X. S.; Belmonte, M. *Opt. Commun.* **1998**, 152, 221–224.
- (40) Bozhevolnyi, S. I.; Hvam, J. M.; Pedersen, K.; Laurell, F.; Karlsson, H.; Skettrup, T.; Belmonte, M. *Appl. Phys. Lett.* **1998**, 73, 1814–16.
- (41) Bozhevolnyi, S. I.; Geisler, T. J. *Opt. Soc. Am. A* **1998**, 15, 2156–62.
- (42) Bozhevolnyi, S. I.; Vohnsen, B.; Pedersen, K. *Opt. Commun.* **1998**, 150, 49–55.
- (43) Smolyaninov, I. I.; Lee, C. H.; Davis, C. C. *Appl. Phys. Lett.* **1999**, 74, 1942–1944.
- (44) Zayats, A. V.; Smolyaninov, I. I.; Davis, C. C. *Opt. Commun.* **1999**, 169, 93–96.
- (45) Smolyaninov, I. I.; Lee, C. H.; Davis, C. C. *Phys. Rev. Lett.* **1999**, 83, 2429–32.
- (46) Jakubczyk, D.; Shen, Y.; Lal, M.; Friend, C.; Kim, K. S.; Swiatkiewicz, J.; Prasad, P. N. *Opt. Lett.* **1999**, 24, 1151–3.
- (47) Zayats, A. V.; Kalkbrenner, T.; Sandoghdar, V.; Mlynek, J. *Phys. Rev. B* **2000**, 61, 4545–8.
- (48) Shen, Y. Z.; Friend, C. S.; Yan, J.; Jakubczyk, D.; Swiatkiewicz, J.; Prasad, P. N. *J. Phys. Chem. B* **2000**, 104, 7577–87.
- (49) Smolyaninov, I. I.; Liang, H. Y.; Lee, C. H.; Davis, C. C.; Aggarwal, S.; Ramesh, R. *Opt. Lett.* **2000**, 25, 835–837.
- (50) Smolyaninov, I. I.; Liang, H. Y.; Lee, C. H.; Davis, C. C. *J. Appl. Phys.* **2001**, 89, 206–211.
- (51) Xie, A. F.; Gu, B. Y.; Yang, C. Z.; Zhang, Z. B. *Phys. Rev. B* **2001**, 63, 4104, U116–U120.
- (52) Smolyaninov, I. I.; Liang, H. Y.; Lee, C. H.; Davis, C. C.; Nagarajan, V.; Ramesh, R. *J. Microscopy* **2001**, 202, 250–254.
- (53) Vohnsen, B.; Bozhevolnyi, S. I. *J. Microscopy* **2001**, 202, 244–249.
- (54) Shen, Y. Z.; Markowicz, P.; Winiarz, J.; Swiatkiewicz, J.; Prasad, P. N. *Opt. Lett.* **2001**, 26, 725–727.
- (55) Jakubczyk, D.; Shen, Y.; Lal, M.; Friend, C.; Kim, K. S.; Swiatkiewicz, J.; Prasad, P. N. *Opt. Lett.* **1999**, 24, 1151–1153.
- (56) Shen, Y. Z.; Swiatkiewicz, J.; Winiarz, J.; Markowicz, P.; Prasad, P. N. *Appl. Phys. Lett.* **2000**, 77, 2946–2948.
- (57) Betzig, E.; Trautman, J. K.; Harris, T. D.; Weiner, J. S.; Kostelak, R. L. *Science* **1991**, 251, 1468–1470.
- (58) Hoffmann, P.; Dutoit, B.; Salathe, R. P. *Ultramicroscopy* **1995**, 61, 165–70.
- (59) Veerman, J. A.; Otter, A. M.; Kuipers, L.; Van Hulst, N. F. *Appl. Phys. Lett.* **1998**, 72, 3115–17.
- (60) Pilevar, S.; Edinger, K.; Atia, W.; Smolyaninov, I.; Davis, C. *Appl. Phys. Lett.* **1998**, 72, 3133–5.
- (61) Girard, C.; Joachim, C.; Gauthier, S. *Rep. Prog. Phys.* **2000**, 63, 893–938.
- (62) Bloembergen, N.; Pershan, P. S. *Phys. Rev.* **1962**, 128, 606–22.
- (63) Berkovic, G.; Superfine, R.; Guyot-Sionnest, P.; Shen, Y. R.; Prasad, P. N. *J. Opt. Soc. Am. B* **1988**, 5, 668–73.
- (64) Keller, O. *J. Microscopy* **2001**, 202, 261–72.
- (65) Betzig, E.; Trautman, J. K. *Science* **1992**, 257, 189–95.
- (66) Vigoureux, J. M.; Girard, C.; Depasse, F. *J. Mod. Opt.* **1994**, 41, 49–58.
- (67) Zhao, X.; Kopelman, R. *Ultramicroscopy* **1995**, 61, 69–80.
- (68) Depasse, F.; Paesler, M. A.; Courjon, D.; Vigoureux, J. M. *Opt. Lett.* **1995**, 20, 234–6.
- (69) Kawazoe, T.; Shimizu, T.; Ohtsu, M. *Opt. Lett.* **2001**, 26, 1687–1689.
- (70) Xie, X. S.; Dunn, R. C. *Science* **1994**, 265, 361–4.
- (71) Ambrose, W. P.; Goodwin, P. M.; Martin, J. C.; Keller, R. A. *Science* **1994**, 265, 364–7.
- (72) Trautman, J. K.; Macklin, J. J. *Chem. Phys.* **1996**, 205, 221–9.
- (73) Lahrech, A.; Bachelot, R.; Gleyzes, P.; Boccara, A. C. *Opt. Lett.* **1996**, 21, 1315–17.
- (74) Zayats, A. V. *Opt. Commun.* **1999**, 161, 156–62.
- (75) Zayats, A. V.; Sandoghdar, V. *Opt. Commun.* **2000**, 178, 245–9.
- (76) Benrezzak, S.; Adam, P. M.; Bijeon, J. L.; Royer, P. *Surf. Sci.* **2001**, 491, 195–207.
- (77) Adam, P. M.; Benrezzak, S.; Bijeon, J. L.; Royer, P.; Guy, S.; Jacquier, B.; Moretti, P.; Montereali, R. M.; Piccinini, M.; Menchini, F.; Somma, F.; Seassal, C.; Rigneault, H. *Opt. Express* **2001**, 9.
- (78) Lee, L. F.; Schaller, R. D.; Haber, L. H.; Saykally, R. J. *Anal. Chem.* **2001**, 73, 5015–5019.

- (79) Ruiter, A. G. T.; Van Der Werf, K. O.; Veerman, J. A.; Garcia-Parajo, M. F.; Rensen, W. H. J.; Van Hulst, N. F. *Ultramicroscopy* **1998**, 149–57.
- (80) Huang, M. H.; Mao, S.; Feick, H.; Yan, H. Q.; Wu, Y. Y.; Kind, H.; Weber, E.; Russo, R.; Yang, P. D. *Science* **2001**, 292, 1897–1899.
- (81) Johnson, J. C.; Yan, H.; Schaller, R. D.; Petersen, P. B.; Yang, P.; Saykally, R. J. *Nano Lett.* In press.
- (82) Jansson, P. A. *Deconvolution of Images and Spectra*, 2nd ed.; Academic Press: San Diego, 1997.
- (83) Hecht, B.; Bielefeldt, H.; Inouye, Y.; Pohl, D. W.; Novotny, L. J. *Appl. Phys.* **1997**, 81, 2492–2498.
- (84) Hong, M. K.; Jeung, A. G.; Dokholyan, N. V.; Smith, T. I.; Schwettman, H. A.; Huie, P.; Erramilli, S.; Huie, P. *Nucl. Instrum. Methods Phys. Res. B* **1998**, 144, 246–55.
- (85) Piednoir, A.; Licoppe, C.; Creuzet, F. *Opt. Commun.* **1996**, 129, 414–22.
- (86) Knoll, B.; Keilmann, F. *Appl. Phys. A* **1998**, A66, 477–81.
- (87) Dragnea, B.; Preusser, J.; Schade, W.; Leone, S. R.; Hinsberg, W. D. *J. Appl. Phys.* **1999**, 86, 2795–9.
- (88) Keilmann, F.; Knoll, B.; Kramer, A. *Phys. Status Solidi B* **1999**, 215, 849–54.
- (89) Knoll, B.; Keilmann, F. *Nature* **1999**, 399, 134–7.
- (90) Michaels, C. A.; Stranick, S. J.; Richter, L. J.; Cavanagh, R. R. *J. Appl. Phys.* **2000**, 88, 4832–9.
- (91) Akhremitchev, B. B.; Pollack, S.; Walker, G. C. *Langmuir* **2001**, 17, 2774–81.
- (92) Dragnea, B.; Preusser, J.; Szarko, J. M.; Leone, S. R.; Hinsberg, W. D. *J. Vac. Sci. Technol. B* **2001**, 19, 142–52.
- (93) Jahncke, C. L.; Paesler, M. A.; Hallen, H. D. *Appl. Phys. Lett.* **1995**, 67, 2483–5.
- (94) Jahncke, C. L.; Hallen, H. D.; Paesler, M. A. *J. Raman Spectrosc.* **1996**, 27, 579–86.
- (95) Webster, S.; Batchelder, D. N.; Smith, D. A. *Appl. Phys. Lett.* **1998**, 72, 1478–80.
- (96) Zeisel, D.; Deckert, V.; Zenobi, R.; Tuan, V.-D. *Chem. Phys. Lett.* **1998**, 283, 381–5.
- (97) Grausem, J.; Humbert, B.; Spajer, M.; Courjon, D.; Burneau, A.; Oswald, J. J. *J. Raman Spectrosc.* **1999**, 30, 833–40.
- (98) Jordan, C. E.; Stranick, S. J.; Cavanagh, R. R.; Richter, L. J.; Chase, D. B. *Surf. Sci.* **1999**, 435, 48–52.
- (99) Ayars, E. J.; Hallen, H. D. *Appl. Phys. Lett.* **2000**, 76, 3911–13.
- (100) Hayazawa, N.; Inouye, Y.; Sekkat, Z.; Kawata, S. *Opt. Commun.* **2000**, 183, 333–6.
- (101) Wang, J.; Yan, H.; Deng, Y.; Li, H.; Zhang, Y.; Zhang, F.; Xia, Z.; Gao, Q.; Du, W.; Zhou, H.; Zou, Y. *Solid State Commun.* **2000**, 115, 173–7.
- (102) Stockle, R. M.; Yung Doug, S.; Deckert, V.; Zenobi, R. *Chem. Phys. Lett.* **2000**, 318, 131–6.
- (103) Hayazawa, N.; Inouye, Y.; Sekkat, Z.; Kawata, S. *Chem. Phys. Lett.* **2001**, 335, 369–74.
- (104) Nieman, L. T.; Krampert, G. M.; Martinez, R. E. *Rev. Sci. Instrum.* **2001**, 72, 1691–9.
- (105) Luo, H.; Furdyna, J. K. *Semi. Sci. Technol.* **1995**, 10, 1041–8.
- (106) Yamada, C.; Kimura, T. *Phys. Rev. B* **1994**, 49, 14372–81.
- (107) Hocker, L. O.; Forbes Dewey, C., Jr. *Appl. Phys. Lett.* **1976**, 28, 267–70.
- (108) Allen, J. W. *Semi. Sci. Technol.* **1995**, 10, 1049–64.
- (109) Queisser, H. J.; Haller, E. E. *Science* **1998**, 281, 945–50.
- (110) Besomi, P.; Wessels, B. W. J. *J. Appl. Phys.* **1982**, 53, 3076–84.
- (111) Karai, M.; Kido, K.; Naito, H.; Kurosawa, K.; Okuda, M.; Fujino, T.; Kitagawa, M. *Phys. Status Solidi A* **1990**, 117, 515–25.
- (112) Du, Q.; Superfine, R.; Freysz, E.; Shen, Y. R. *Phys. Rev. Lett.* **1993**, 70, 2313–16.
- (113) Belin, M. A.; Han, S. H.; Wei, X.; Shen, Y. R. *Phys. Rev. Lett.* **2001**, 87, 113001.
- (114) Simonelli, D.; Shultz, M. J. *J. Chem. Phys.* **2000**, 112, 6804–16.
- (115) Gracias, D. H.; Zhang, D.; Lianos, L.; Ibach, W.; Shen, Y. R.; Somorjai, G. A. *Chem. Phys.* **1999**, 245, 277–84.
- (116) Rasing, T.; Hung, J.; Lewis, A.; Stehlin, T.; Shen, Y. R. *Phys. Rev. A* **1989**, 40, 1684–7.
- (117) Scatena, L. F.; Brown, M. G.; Richmond, G. L. *Science* **2001**, 292, 908–12.
- (118) Baldelli, S.; Eppler, A. S.; Anderson, E.; Shen, Y. R.; Somorjai, G. A. *J. Chem. Phys.* **2000**, 113, 5432–8.
- (119) McGuire, J. A.; Beck, W.; Wei, X.; Shen, Y. R. *Opt. Lett.* **1999**, 24, 1877–9.
- (120) Richter, L. J.; Petralli-Mallow, T. P.; Stephenson, J. C. *Opt. Lett.* **1998**, 23, 1594–6.
- (121) Ishibashi, T.; Onishi, H. *Chem. Phys. Lett.* **2001**, 346, 413–418.
- (122) Bonn, M.; Hess, C.; Funk, S.; Miners, J. H.; Persson, B. N. J.; Wolf, M.; Ert, G. *Phys. Rev. Lett.* **2000**, 84, 4653–6.
- (123) Hess, C.; Bonn, M.; Funk, S.; Wolf, M. *Chem. Phys. Lett.* **2000**, 325, 139–45.
- (124) Hess, C.; Wolf, M.; Bonn, M. *Phys. Rev. Lett.* **2000**, 85, 4341–4.
- (125) Hess, C.; Funk, S.; Bonn, M.; Denzler, D. N.; Wolf, M.; Ertl, G. *Appl. Phys. A* **2000**, A71, 477–83.
- (126) Briggman, K. A.; Stephenson, J. C.; Wallace, W. E.; Richter, L. J. *J. Phys. Chem. B* **2001**, 105, 2785–2791.
- (127) Shimanouchi, T. *Tables of Molecular Vibrational Frequencies*; National Bureau of Standards: Washington, 1972.
- (128) Chestnoy, N.; Hull, R.; Brus, L. E. *J. Chem. Phys.* **1986**, 85, 2237–42.
- (129) Nguyen, T.-Q.; Schwartz, B. J.; Schaller, R. D.; Johnson, J. C.; Lee, L. F.; Haber, L. H.; Saykally, R. J. *J. Phys. Chem. B* **2001**, 105, 5153–5160.
- (130) Schaller, R. D.; Johnson, J. C.; Lee, L. F.; Haber, L. H.; Saykally, R. J.; Nguyen, T.-Q.; Schwartz, B. J. Submitted for publication.
- (131) Johnson, J. C.; Yan, H.; Schaller, R. D.; Haber, L. H.; Saykally, R. J.; Yang, P. *J. Phys. Chem. B* **2001**, 105, 11387–90.
- (132) Parkanyi, C.; Boniface, C.; Aaron, J. J.; Maafi, M. *Spectrochim. Acta A* **1993**, 49, 1715–25.
- (133) Cordone, L.; Cupane, A.; Leone, M.; Vitrano, E. *Biophys. Chem.* **1986**, 24, 259–276.